Simultaneous near-infrared and visible observations of sprites and acoustic-gravity waves during the EXL98 campaign

Carl L. Siefring,[1] Jeff S. Morrill,[2] Davis D. Sentman,[3] and Matthew J. Heavner[4]

[1]   This paper reports the first images of Near-InfraRed (NIR) 900 to 1700 nm sprite emissions obtained during the Energetics of Upper Atmospheric Excitation by Lightning 1998 (EXL98) airborne observing mission. Results include the first NIR observations of sprites and a correlation between nighttime hydroxyl (OH) airglow, acoustic-gravity waves, and sprite location. A NIR camera monitored both OH airglow and $N_2(B)$ First Positive (1PG) emissions in the NIR by sprites. OH airglow is used as a tracer of acoustic-gravity waves and density structures in the neutral atmosphere in the 80–95 km altitude region. The visible-light imager also observed faint hydroxyl airglow, at times, allowing convenient comparison of the gravity waves and the sprites without image processing. On only one night of observations was a clear correlation observed between the OH airglow and the sprites, with tops of extended lines of sprites appearing to align with the acoustic-gravity wave troughs in the 80 to 95 km altitude region. This investigation shows that a proper viewing geometry is needed to detect such a correlation and requires a distance of about 400–800 km from the sprites. Comparison of sprite visible and NIR emissions show that the NIR is brightest in the central body, likely dimmer at the tops, and rarely above sensitivity in the tendril regions. The observed NIR sprite emissions are thought to be primarily 1PG from the (1,0) and (0,0) vibration transitions near 888 and 1050 nm respectively. The study indicates a need for future NIR spectrographic measurement.

1.   Introduction

1.1.   EXL98

[2]   During the summer of 1998, airborne observations of sprites, elves and blue jets were made during the University of Alaska led EXL98 (Energetics of Upper Atmospheric Excitation by Lightning, 1998) campaign. The EXL98 Campaign ran the two-weeks of July 15–29, 1998, performing nighttime observations in moon-down conditions. The primary goal of EXL98 was to investigate the sprite energy budget by remote sensing of various portions of the optical spectrum, including emissions in the near ultraviolet (NUV), visible, near infrared (NIR), and medium infrared (MIR) wavelengths that cannot be easily observed on the ground. Simultaneous sprite observations were obtained using eight separate low-light-level imaging systems from a Gulfstream II jet aircraft. Ground sites were operated at Wyoming InfraRed Observatory (WIRO) at Mt Jelm, WY, and at Mt Evans, CO.

[3]   In-field flight operations were conducted out of Jefferson County (JEFFCO) airport near Boulder, CO, but the ferry flight from Hillsboro, OR to JEFFCO was also used for observations. Missions were flown over the Great Plains states when large frontal storms were deemed likely to continue into the night. Weather forecasts and the National Lightning Detection Network (NLDN) were used for determining storm locations and making Go/No-Go decisions for the nighttime missions. Timing synchronization between the ground and airborne observations was coordinated using GPS (Global Positioning Satellite) technology. Further details of the experimental campaign are given by *Heavner* [2000].

[4]   Figure 1 and Table 1 illustrate the EXL98 Gulfstream II jet aircraft measurement configuration. The aircraft carried a suite of 8 separate co-aligned low-light level systems with spectral responses covering a wide range of wavelengths 340 nm to 4.3 microns. The NUV camera, instrument 5, in Table 1, was operated as either a filtered imager or as a spectrograph. Several results from the mission have already been published. *Morrill et al.* [2002] used filtered images of N_2^+ Fist Negative and N_2 Second Positive emissions to estimate the electric fields versus altitude causing the sprite breakdown. *Wescott et al.* [2001] and *Heavner*

[1]Plasma Physics Division, Naval Research Laboratory, Washington, D. C., USA.

[2]E. O. Hulburt Center for Space Research, Naval Research Laboratory, Washington, D. C., USA.

[3]Geophysical Institute, University of Alaska Fairbanks, Fairbanks, Alaska, USA.

[4]Los Alamos National Laboratory, Los Alamos, New Mexico, USA.

Figure 1. EXL98 Gulfstream II aircraft and NIR camera. (top left) The aircraft, with the specialized windows covered for protection when not in flight. (top right) Two of the quartz windows. In the left window the Color, Wide FOV and Narrow FOV cameras are mounted and in the right window the NIR and NUV imagers. The center window is the standard Gulfstream Plexiglass. (bottom left) The interior of the aircraft; observations could only be made out of the left-hand side. (bottom right) The NIR imaging camera.

et al. [2000] similarly explore ionization in blue starters using the filter measurements. Finally, *Heavner et al.* [2010] analyzes the blue/NUV spectra taken with the NUV spectrograph.

[5] The visible, NIR and NUV sensors looked out of quartz windows that were installed in the Gulfstream II (Figure 1). They were co-aligned on the ground at zero-degrees elevation, by observing distant objects. All camera mounts had stops at 0°, 5°, 10°, and 15° for setting elevation; however all of the observations were taken with the elevation at either 0° or 5°. Figure 1 shows the visible cameras looking out of one window and NIR and NUV a second window located about 2 m apart. No effort has been made to correct for parallax as most of our sprite observations are viewing objects at greater than 100 km distance. The Fields-of-View (FOV) of each camera (Table 1) were derived in two ways. For the intensified visible-light cameras star fields were used. The NIR and filtered cameras were then compared with the narrow-FOV visible camera using simultaneous images of distant bright lights taken from the Hillsboro runway. The television systems used are drop-frame NTSC (National Television System(s) Committee) standard systems which run at 29.97 frames per second. A Horita timing system provided a time stamp,

Table 1. Summary of Instrumentation on the EXL98 Campaign Gulfstream II Aircraft

|	Instrument Description	Optical Range	λ	Emissions Observed	FOV (deg) (H × V)	A/C Viewport Material
1	broadband wide FOV scene camera	visible	400–740 nm	sprite N_2, blue starters	55 × 43	quartz
2	color camera	visible	400–700 nm	sprite N_2, blue starters	~15 × 12	quartz
3	broadband narrow FOV camera	visible	400–740 nm	sprite N_2, blue starters, OH airglow	9.3 × 7	quartz
4	N_2^+ first negative filtered narrow FOV camera	blue	427.8 nm	N_2^+ first negative from sprites and blue starters	9.3 × 7	quartz
5a	N_2 second positive filtered NUV imager	NUV	337.0 nm	N_2 second positive from sprites and blue starters	10.8 × 8	quartz
5b	NUV spectrograph	NUV-visible	300–460 nm	N_2 second positive and N_2^+ first negative sprite spectra	10.8 × 0.2	quartz
6	NIR imager	0.9–1.7 μm	0.9–1.7 μm	sprite N_2 first positive, OH airglow, blue starters	11 × 11	quartz
7	MIR radiometer	2.7 μm	2.7 μm	none	~1 × 1	CaF
8	MIR image AMBER	4.3 μm	4.3 μm	none	~20 × 20	CaF
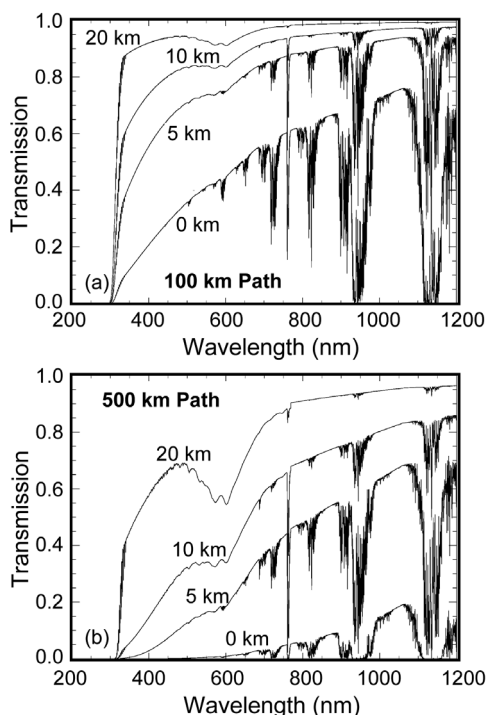
Figure 2. The atmospheric transmission curves motivate why the EXL98 measurements required an airborne platform. (a) A 100 km total path length with curves given for an observer at 0, 5, 10 and 20 km altitude. (b) The same for a 500 km path. Note the attenuation in the NUV (300–400 nm) and the NIR (>900 nm).

using SMPTE (Society of Motion Picture and Television Engineers) time code standard and a common sync pulse for all video cameras. Furthermore the Horita system used GPS for timing. The use of multiple Horita systems allowed for spatially separated camera systems (e.g., the aircraft and the ground based sites at Mt. Evans and WIRO) to be sync-locked. The video images along with timing information were recorded on Sony U-Matic 3/4″ standard video format tape recorders. All images presented are post-mission video captures, from videotape, using a PC-based image capture system.

1.2. Simultaneous NIR and Visible Observations

[6] The EXL98 observations included a NIR (900-1700-nm) sensitive camera supplied by the Naval Research Laboratory (NRL) using a relatively new (at the time) technology Indium-Gallium Arsenide (InGaAs) focal-plane array (128 × 128 pixels). The InGaAs camera has a high Quantum Efficiency >65%, but is not intensified and takes advantage of the relative brightness of the hydroxyl airglow in the NIR (Figure 3). A high-speed f/0.9, 25 mm lens was used, yielding approximately an 11° × 11° FOV. It was designed to monitor hydroxyl airglow, which gives indications of density variations and structure in the neutral atmosphere, e.g., acoustic-gravity waves. Gravity waves are known to be associated with thunderstorms [cf. *Sentman et al.*, 2003; *Taylor and Hapgood*, 1988; *Taylor et al.*, 1991]. In addition, the NIR imager was used to look for N_2 First Positive Group (1PG) emissions in the NIR. Previous

spectrographic measurements have shown that the red N_2 1PG are the brightest emissions in sprites [cf. *Mende et al.*, 1995; *Hampton et al.*, 1996; *Morrill et al.*, 1998; *Bucsela et al.*, 2003]. Much of the N_2 1PG $\Delta V < 2$ emissions are in the NIR wavelengths.

[7] The NIR images will be compared to a narrow-FOV intensified imager supplied by the University of Alaska. It is one of the cameras used in previous sprite campaigns, e.g., *Sentman et al.* [1995]. This Dage-MTI VE-1000 Silicon-Intensifier Target (SIT) tube B/W camera has a sensitivity of 1.6×10^{-7} W-m^{-2} at 550 nm and 750 lines/in resolution. The 3 db bandpass of the Dage-MTI camera is approximately 425 nm to 625 nm but has a response that extends out to ~740 nm on the red end. A fast f/0.85 Fujinon 45 mm c-mount lens was used which yielded a FOV of 9.3° × 7°. Somewhat serendipitously, this highly intensified white-light camera was also able to observe the hydroxyl airglow. The white-light camera, if operated near the highest gain, could observe the sprites on top of a faint OH airglow background, which resulted in the best comparison between the two phenomena using unprocessed images. In the case of the NIR images, the OH background was extremely bright and would have required image processing to highlight the sprites.

1.3. Atmospheric Transmission

[8] Atmospheric absorption and scattering plays a large role in determining what can be learned of Sprite and other TLE (Transient Luminous Events) energetics using only ground based techniques. Figure 2 illustrates the advantage of using an airborne platform. A good comparison to make is a mountain top observer versus an airplane observer. The mountain-based observer would be at about 5 km altitude and have no control over the observing path length. In EXL98, the Gulfstream II service ceiling was about 13.5 km (44 kft) and the aircraft could fly to any storm location within round trip range. Comparing the transmissions for 10+km altitude and 100 km path (airborne) to 5 km altitude and 500 km path, it is clear why the aircraft is extremely advantageous. For example, at the principle transition (0–0) of the N_2 Second Positive Group (2PG) at 337 nm almost no emissions survive atmospheric transmission to the mountain top observer, while ~60% of the emission can be seen by the aircraft observer. It is somewhat better in the NIR, but there are several water absorption bands that affect observations made from mountain-top altitude sites. The situation for 1PG emissions in the NIR is also improved with aircraft observations where strong 1PG bands between 1000 and 1200 nm are more easily observed.

1.4. Hydroxyl Airglow

[9] The airglow from OH emissions is generated by one or more luminescent chemical reactions between minority constituents in the mesosphere. The primary reaction is believed to be

$$H + O_3 \rightarrow OH(X^2\Pi)\left(v' \leq 9\right) + O_2 + 3.34 \text{ eV} \qquad (1)$$
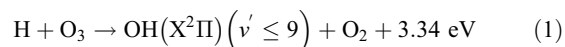
[*Chamberlain*, 1995] although others have been suggested to contribute [*Sharma*, 1985; *Chamberlain*, 1995] and some of the radiative and quenching lifetimes are not well known
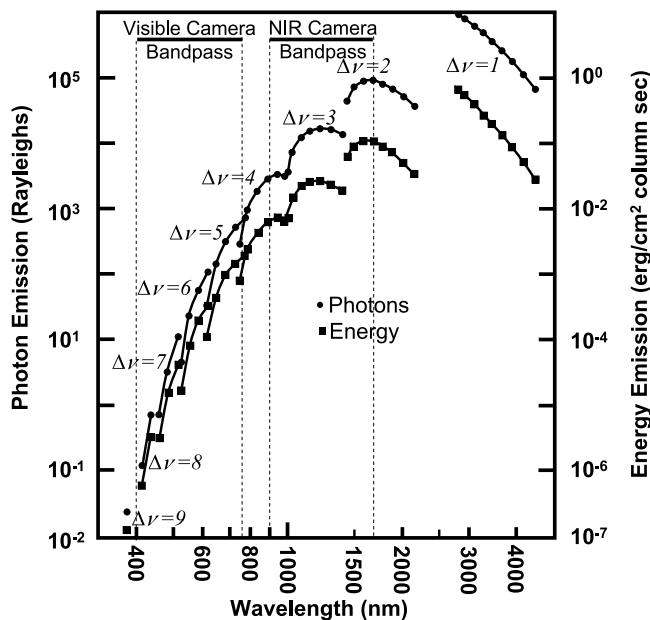
Figure 3. Predicted hydroxyl emission for vertical observations and the approximate bands for two of the EXL98 cameras.

[e.g., *Llewellyn et al.*, 1978]. The reactions generate strong airglow with very bright emissions from the OH (XΠ $\Delta v = 2,3$) complexes between 1.0 μm and 2.2 μm. Because O_3 densities are extremely small above about ~80 km and H concentration is small at low altitudes the OH airglow originates from a narrow band of altitudes peaking at ~87 km with a half-width of 5–8 km [*Baker and Stair*, 1988].

[10] Figure 3 shows an estimated OH spectrum looking vertically through the atmosphere (recreated from *Chamberlain* [1995]) where the approximate passbands of the two cameras that detected the airglow during the EXL98 flights are also indicated. OH observations were made at low elevation angles, which increase the path length in the airglow region. The elevation look-angle affects the measured brightness; from the aircraft observing at 0° elevation the depth-of-layer is about seven times greater than looking vertically. This reduces to a factor of six at 5° and four at 10° elevation. As shown in Figure 2, atmospheric absorption can also have an effect on the observation of the hydroxyl airglow especially at long path lengths. Combined these characteristics allowed for observing the OH airglow at a video rate (30 frames/s) on all flights. This is important as aircraft motion and vibration preclude integrating for a long time as is possible on the ground.

[11] Acoustic-gravity waves are low frequency atmospheric buoyancy waves. Disturbances that introduce a change in the atmosphere on a time scale of few-minutes to several-hours may be capable of generating upward propagating gravity waves. Strong weather systems like jet streams, fronts, tornadoes, thunderstorms [e.g., *Hines*, 1968; *Röttger*, 1977; *Freund and Jacka*, 1979; *Hung et al.*, 1979; *Taylor et al.*, 1995; *Taylor and Hapgood*, 1988], and even winds blowing over mountain ranges [e.g., *Eckermann and Preusse*, 1999] can be sources for gravity waves. The physics of thunderstorm convection generated gravity waves is quite complex and horizontal wavelengths can vary over a

wide range [cf. *Taylor et al.*, 2009; *Vadas et al.*, 2009, and references therein]. *Taylor et al.* [2009] show observations in Brazil with horizontal wavelengths λ_h varying from 20 km to a little over 300 km although this paper does not tie these observations directly to convective storms.

[12] Variations in the neutral density near about 78–95 km strongly affect the OH airglow because the emission rate is dependent of $(\Delta N/N)^2$. In addition, upward propagating gravity waves increase in amplitude ($\Delta N/N$) as the atmospheric density decreases, in order to maintain the same wave energy, and reach maximum amplitudes at mesospheric/D-region altitudes where nonlinear effects, such as wave breaking, can occur. More details are given by, e.g., *Walterscheid et al.* [1994] that presents a comparison of gravity wave theories and the fluctuations they induce in the airglow layer, and *Tarasick and Shepherd* [1992a, 1992b] that incorporates relatively sophisticated chemical schemes for the reacting airglow species.

1.5. Possible Correlation Between Acoustic-Gravity Waves and Sprites

[13] Avalanche breakdown models of sprites indicate that ionization rates are highly dependent on the neutral density. *Fernsler and Rowland* [1996], *Pasko et al.* [1997a], and *Rowland* [1998] have predicted that gravity waves may affect the location and filamentation of sprites and cause brightness variations in elves [*Rowland et al.*, 1996]. In the *Rowland* [1998] and *Fernsler and Rowland* [1996] models an empirical fit to laboratory measured ionization rates in air for E/N is used and gives

$$\gamma \sim 10^{-8} Ne^{-960N/E} \qquad (2)$$

as the ionization rate where E/N is in Townsends (1 Td = 10^{-17} V-cm^2) and where the electric field amplitude is bounded by approximately 120 Td < E/N ≤ 370 Td which corresponds roughly to 1 to 3 times the breakdown field. *Pasko et al.* [1997b] did a cross-comparison between more complicated Boltzmann-solving sprite models and those using empirical fits to laboratory data and found generally good agreement between the two methods. This steeply dependent exponential ($e^{-960N/E}$) is the reason that local neutral density variations are postulated to effect the formation of sprites and provides a natural way to account for horizontal offset of sprite initiation relative to the underlying parent thunderstorm [e.g., *Sao Sabbas-Tavares*, 2003].

[14] The electric field bounding can be understood as follows. First, at low field amplitudes the measured ionization rate effectively goes to zero as electron attachment is faster than the production of ionization. Second, when electric field becomes large a great quantity of ionization is produced which acts to quickly shield out the electric fields. Thus, the fields are self-limiting and typically will not exceed 200 Td in a sprite [*Rowland*, 1998]. Furthermore, this process and electric field focusing leads to streamer formation which is thought to be needed to achieve breakdown at the lower altitudes (~55 km and below) of sprites [cf. *Pasko et al.*, 1998; *Raizer et al.*, 1998].

[15] At the altitudes where sprites form, we can have pre-existing gravity waves possibly generated by convective processes in the storm itself. Assuming an E/N = 130 Td with an average neutral density of N = 2.84 × 10^{14}cm^{-3}
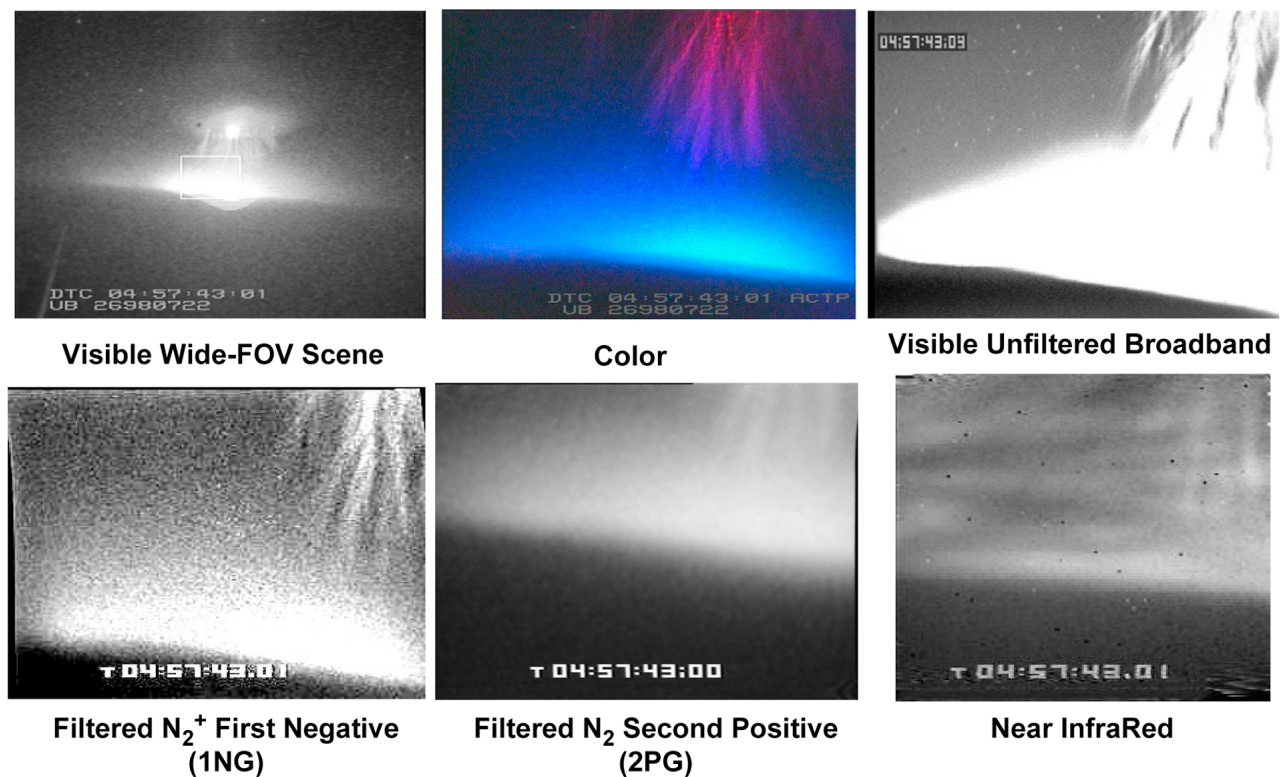
Figure 4. Samples from six imagers from EXL98 (see text for discussion).

(a 36.9 V/m field at ~80 km altitude) the ionization rate for N+5% is 1280 electrons/s and for N−5% is 2420 electrons/s, a factor of ~2 in ionization rate with only a 10% peak-to-peak modulation. Thus, the ionization rate can be significantly higher in the troughs of the gravity wave and smaller in the crests.

2. Data Presentation

2.1. Multiple Camera Observations

[16] Figure 4 shows sample images from six of the EXL98 cameras, each imager has it own FOV as listed in Table 1. Figure 4 (top left) is the 55° H × 43° V wide-FOV visible-light scene-camera. This camera shows a large sprite, with halo and tendrils that extend into the scattered light near the cloud tops. The white box drawn in this image indicates approximately the view of the other cameras. The box is an exact match for the FOV of the unfiltered broadband visible camera (Figure 4, top right) and a filtered visible camera looking at N_2^+ First Negative (1NG) emissions. The color camera (Figure 4, top middle) has a slightly larger FOV. The next two images are from the NUV filtered camera looking at N_2 Second Positive Group (2PG) emissions (Figure 4, bottom middle) and the NIR camera (Figure 4, bottom right). The filtered 2PG camera has about the same horizontal FOV as the box but with a slightly different aspect ratio, while the NIR camera FOV is somewhat larger. The NUV and NIR cameras were tilted down 5° with respect to the other cameras for these images. The two MIR instruments (see Table 1) did

not report any emissions that were obviously above the background and are not included on here.

[17] A number of the characteristics, some common and some uncommon, are seen in the images of Figure 4. The 55° FOV image (Figure 4, top left) shows a sprite complex with halo. There is a large amount of scattered light from the cloud tops. All other narrower FOV imagers show the tendril regions of the sprite. This specific example was extremely bright with both the scattered light from the cloud tops and tendrils saturating the images for several frames. Although the evidence was not conclusive, these images suggested the possibility that the tendrils reached down to the cloud tops [*Bowles et al.*, 1998] in this case.

[18] For this paper the characteristics of the NIR image are important. The tendrils are very faintly visible in Figure 4 (bottom right) and there may be some enhancement in the light level from the cloud tops. The reduction in scattered light in the NIR is sensible as atmospheric scattering is more severe for blue light. This is one of the few cases where the tendrils are detected in the NIR. The NIR image is filled with bright OH airglow emissions in the background that originate from 80 to 95 km and appear quite structured. The somewhat layered look for the OH emissions could be generated by a set of wavefronts the start nearby and continues farther away until merging at the horizon. In the image, the emissions are seen in projection with the OH airglow distributed horizontally in the background and the tendrils extending vertically in the foreground. There also appear to be some shorter scale wave structures in the image.

Figure 5. Samples of Hydroxyl (OH) airglow from one day of the EXL98 campaign show a great variability in the structure of the airglow. The top two images are from July 15, 1998 and the bottom four images are from July 28, 1998.

2.2. NIR Hydroxyl Airglow

[19] Figure 5 shows a sample of airglow observations from six frames from the NIR camera. Each frame displays a portion of the atmosphere at 85 km altitude that is about an 800–1000-km rectangle. These frames illustrate a good variety of the conditions observed during the EXL98 mission and could be described as typical variability for gravity wave features (cf. descriptions given by *Roach and Meinel* [1955]). Figure 5 is included because we could not find published images of the typical variations, especially when viewing at low elevation angles. Figure 5 (top) shows very well structured airglow similar to those that are reported in gravity wave studies such as *Taylor et al.* [1995]. We interpret these long airglow features as arising from a single large source, possibly a frontal system. The next two frames show airglow that looks to be a mixture of waves from different sources, and we might characterize the atmosphere at the airglow altitudes as being 'choppy'. In a number of the images, the airglow is faint at the upper edge of the frame and very bright at the bottom of the frames. As described earlier, observing at a low elevation angles is the most probable cause of this intensity distribution. The final frame (lower-right) shows a case where there is very little variation in the airglow and in order to display the variation it is necessary to increase the contrast of the frame dramatically. The almost black portion at the bottom of some

of the frames is the cloud tops that were generally dark in the NIR. When the NIR camera was tilted up the airglow starts to become too faint to observe at video rates at about 25° elevation.

[20] Throughout the EXL98 flights, spatially structured OH airglow was the most common feature whereas only a small fraction of the data shows the very weak airglow modulations displayed in Figure 5 (bottom right). From the moving aircraft it was easy to differentiate modulations in the airglow intensity and effects caused by occasional intervening high cirrus clouds. The OH airglow would be constant over many minutes, whereas the plane would move quickly through a band of cirrus clouds in several seconds.

2.3. Sprites in the NIR and Visible

[21] Figure 6 shows a sample of the simultaneous observations of NIR and visible emissions generated by sprites (Figure 6, top left). Figure 6 (bottom left) shows the corresponding white-light image. The white-light image has been reduced in size so that the images can be overlaid and represent the proper portion of the wider FOV NIR camera (accuracy is about 1%). From the white-light image we can see that there are four sprites, while three sprites are clearly visible in the NIR image with only a hint of the fourth, on the left. We note the much poorer pixel-resolution of the NIR camera (only 128×128 pixels) compared the white-light camera (640×480 in the capture) accounts for the lack of details in the later image. In Figure 6 (bottom right), a contour map of intensity is made from the visible image and then overlaid onto the NIR image in Figure 6 (top right).

[22] The image is typical of the sprite emissions seen in the NIR during the EXL98 campaign. The central portions of the sprites are brightest in the NIR with the tops significantly fainter. The lower portions of the sprites, normally
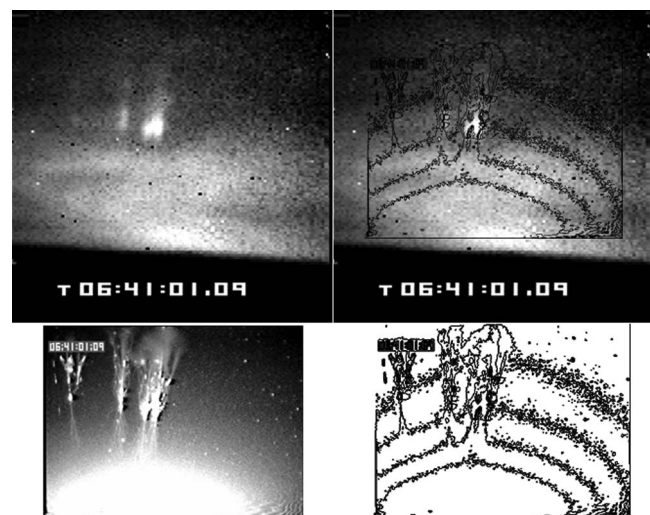

Figure 6. Sample comparison of visible and NIR observations of sprites from 7/18/1998. The frame sizes have been adjusted for FOV differences. (top left) The NIR image, which shows both sprite emissions and OH airglow. (bottom left) The visible image. (bottom right) A contour map of the brightness of the visible image and (top right) the contour map overlaid onto the NIR image.
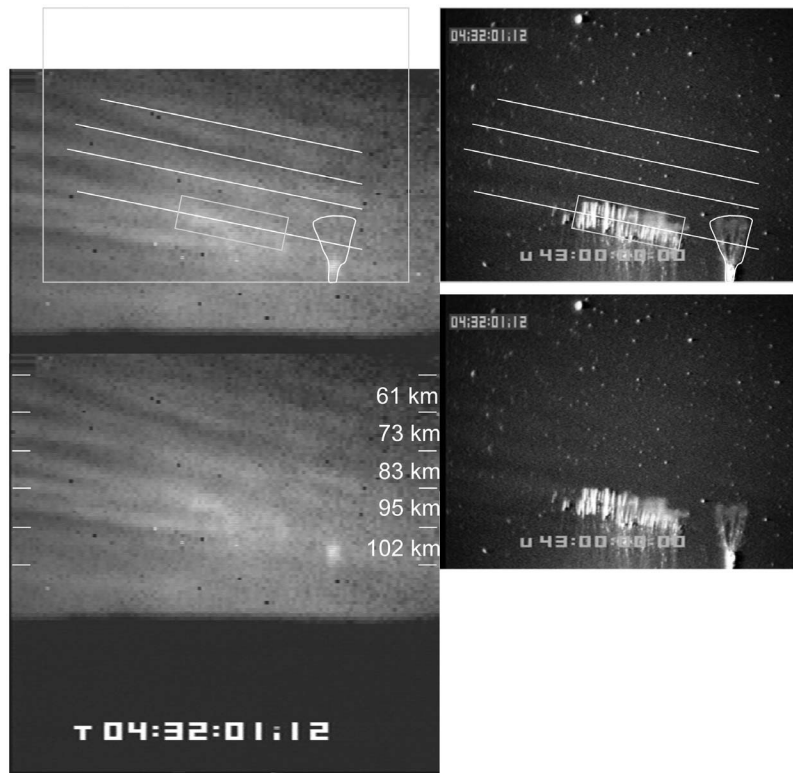
Figure 7. Sprites and OH Airglow in both the NIR and the visible wavelengths. (left) The NIR image and (right) the visible. The top images have several features highlighted for comparison. The bright and well structured OH airglow dominates the NIR image and can be seen, faintly, in the visible image. While the sprites are the brightest objects in the visible but faint in the NIR. The tops of the sprites appear to align with the troughs of the acoustic-gravity wave induced airglow structure. The approximate distances noted on the right side of Figure 7 (bottom left) are the vertical projection of the length along the airglow layer for each one-degree increment. These can be used to estimate horizontal wavelengths from the vertical dimensions of the structures. See text for more detail.

bluish and filamented [e.g., *Gerken et al.*, 1998; *Suszcynsky et al.*, 1998; *Heavner et al.*, 2000], are either not present or are masked because of the ambient OH airglow. Sometimes it was not possible to locate a sprite in the NIR image when one occurred in the visible. The contour overlay makes it clear how little scattered light is present in the NIR image. There seems to be a trend in the comparison of the NIR and visible images where the ratio of the (central) core-to-top brightness is greater in the NIR than in the visible. Unfortunately, this is difficult to quantify as the visible images almost always have a portion in the central core that is saturated.

2.4. Sprites and Acoustic-Gravity Wave Correlation

[23] Figure 7 shows sprites and OH airglow in both the NIR (Figure 7, left) and the visible wavelengths (Figure 7, right). The images in Figure 7 (top) have several features highlighted for easy comparison. The bright and well structured OH airglow dominates the NIR image and can be seen, faintly, in the visible image. While the sprites are the brightest objects in the visible they are faint in the NIR. The tops of the sprites appear to align with the troughs of the acoustic-gravity wave induced airglow structure. The emissions from the tops of the sprites would come from the same altitude as the airglow emissions ~85 km or higher [cf. *Sentman et al.*, 1995]. A vertical scale is placed in Figure 7 (bottom left) to help estimate the horizontal wavelength (λ_h) of the gravity waves. The tick marks correspond to one degree increments in the line-of-sight. The distances noted approximate the length along the airglow layer, of the portion of the sky viewed in each one-degree increment. The distances are calculated as follows: 1) Each line-of-sight is projected from 14 km altitude (airplane) until it intersects 90 km altitude; 2) The length of the line segments connecting these intersections is calculated. The bottom tick is assumed to be the local horizontal (i.e., the airplane is flying level) and an Earth Radius of 6371 km was assumed. Because of the viewing geometry a larger patch of sky is observed at lower elevations. It appears the λ_h of the gravity waves is near 70 km with some features having a smaller scale size.

[24] Figure 8 shows more sample frames from two intervals on July 15, also available as Movies 1 and 2.[1] Figure 8 (top) shows the gravity wave structures before the sprites occur and Figures 8 (middle) and 8 (bottom) show two samples of sprites in the time intervals. The alignment is not
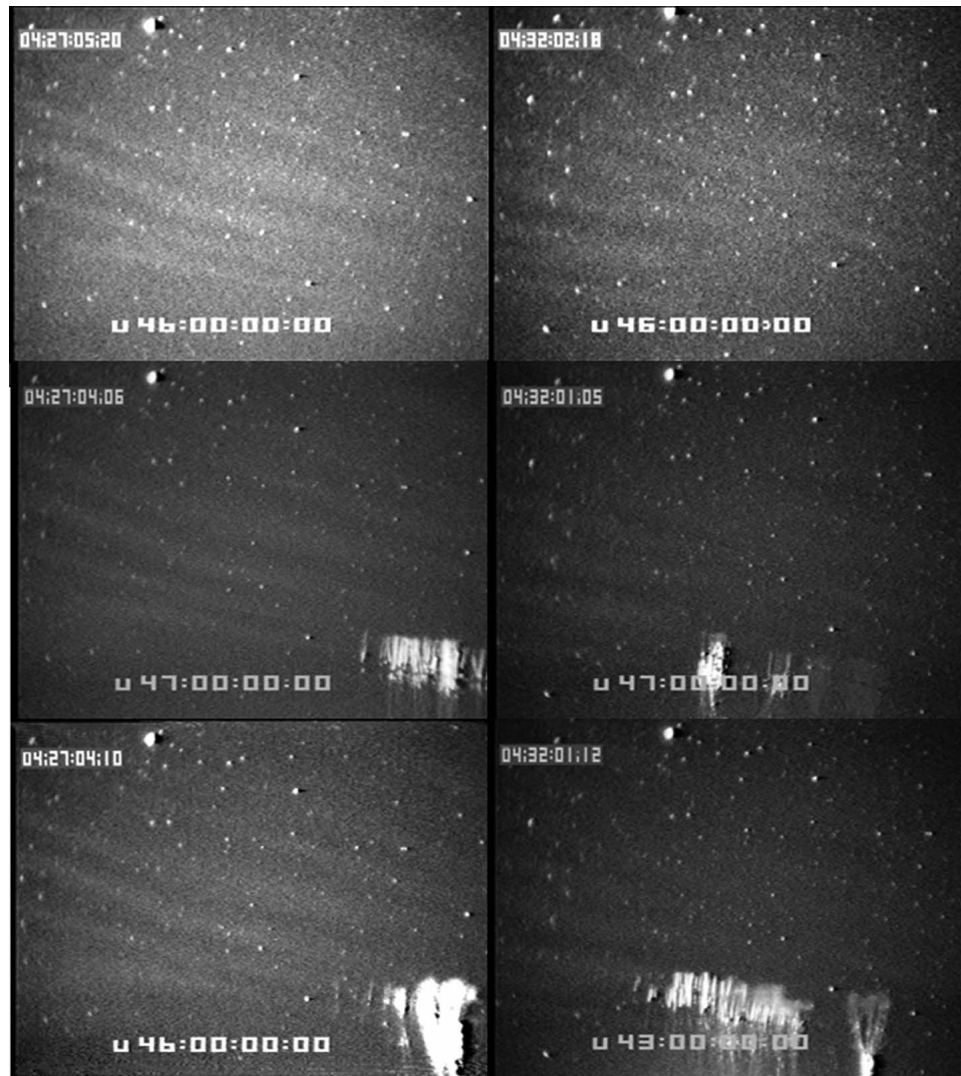
---

[1]Animations are available in the HTML.

Figure 8. Visible wavelength images from July 15, 1998. The only day during the EXL98 campaign where there was a clear correlation seen between the gravity wave structures and the sprite locations. See also Movies 1 and 2.

always perfect as the diffuse upper portion of the sprites sometimes appear to fill a larger area than the troughs in the background airglow. The groups of sprites centered horizontally in the image in Figure 7 look similar to c-sprites with some tendril development, but they may be fully developed sprites just viewed from a large distance. The data was taken on July 15, 1998, which was the ferry flight from Oregon to Colorado. Figure 9 shows maps corresponding to the July 15, 1998 UT observations shown in Figures 7 and 8. Each map shows National Lightning Detection Network (NLDN) cloud-to-ground flash data where positive flashes are dark and negative flashes are white. Figure 9 (top) shows six minutes of NLDN data from 04:27:00 to 04:33:00 and gives an indication of the active thunderstorm size, which spans the State of Minnesota. Figure 9 (middle) shows three seconds of data from the 04:27:03 to 04:17:06. Figure 9 (bottom) shows two seconds of data from 04:32:00 to 04:32:02. These times correspond to the samples shown in Figure 8. The Aircraft location and

an eleven degree FOV are indicated. The two white lines showing the FOV are 800 km in length and indicate an approximate range from the sprites.

3. Discussion

3.1. NIR and Acoustic-Gravity Waves

[25] The series of sprites and particularly strong and well-structured airglow emissions in Figure 8 was observed with the narrow-FOV visible camera. The advantage of this image is that it does not require any processing to show the relationship between the hydroxyl airglow and the sprites. The brightness decreases toward the edges of the frame because of rather severe vignetting, a result of the fast lens (f/0.85) used with the camera system. However, it is relatively clear that the tops of the sprite 'columns' are aligned along one the 'rows' of the ambient airglow. The fact that the visible imager is intensified and has a response that extends to nearly 740 nm on the red-end may explain why

Figure 9. Maps for the July 15, 1998 UT observations shown in Figures 7 and 8. Each map shows NLDN data where positive flashes are dark and negative flashes are white. (top) Six minutes of NLDN data from 04:27:00 to 04:33:00 and gives an indication of the active thunderstorm size. (middle) Three seconds of data from the 04:27:03 to 04:27:06. (bottom) Two seconds of data from 04:32:00 to 04:32:02. These times correspond to the samples shown in Figure 8. The Aircraft location and an eleven degree FOV are indicated. The two white lines showing the FOV are 800 km in length.

the airglow was detectible (see Figure 3, which shows the OH brightness increasing with longer wavelength). On this particular day (July 15) this type of correlation between the sprites and the nightglow was common, with more than a couple of dozen examples captured.

[26] It is interesting that there was only one observing day (July 15), the first day of the EXL98 campaign, where this correlation between the sprite (tops) locations and the airglow was clearly discernable. This is true even though there were several nights with clearly structured airglow similar to the July 15 observations. There were some differences between the first couple of days of observations and the later observations. It was realized that the N_2 filtered 2PG measurements at 337 nm were being severely degraded by flying 400–500 km away from the storms. This can be seen by examining the transmission at 337 nm for 500 km and 100 km path lengths and ~13 km altitude in Figure 2. Only about 20% of the emission reaches an aircraft with a 500 km path, while about 80% of the emission reaches an aircraft with a 100 km path. As a result, a decision was made to fly closer (~100 km) to the thunderstorms on subsequent flights. There was some concern that air traffic control would not give permission to fly this close, but as there were no other aircraft within 500 km of the storms, we were given free reign to approach the storms as near as was deemed to be safe.

[27] Since the EXL98 aircraft campaign, another similar set of measurements was taken from the ground by *Sentman et al.* [2003]. These observations showed that the concentric rings of OH airglow were observed to originate from a severe thunderstorm. However, as with the majority of the EXL98 observations, no clear correlation between the sprites and the gravity wave structures was seen by *Sentman et al.* [2003].

[28] Figure 10 illustrates that a favorable viewing geometry is important with about 400 km to 800 km distance being ideal. Figure 10 is drawn to scale and shows the effect the curved Earth has on the observations. The nightglow is confined to a narrow range of altitudes centered around 87 km, which is approximately the same altitude as the tops of the sprites. It is important that the cameras observe sprites with tops at the same altitude as the airglow layer. If observing far away from the storm, e.g., the sprites drawn at 500 to 800 km distance, the tops of sprites are in view and the airglow is bright because of the long path length through the layer. It is thus possible to see the airglow structures and the sprite top alignment. This explains the lack of correlations when observing at closer distances. If observing too close to the storm, e.g., the sprite drawn at 200 km distance, the camera needs to be tilted up to see the tops of the sprite and the airglow becomes very faint. From the aircraft, where video rate observations are needed because of the motion and vibration of the aircraft, the airglow became too faint to be seen at greater than about 25° elevation. Thus it was not possible to observe the alignment when looking for sprites at close range. Finally, looking further into the distance and low on the horizon the airglow structures merge together and again the effect is not observable. It should be noted that ground-base observations can view the airglow at higher elevations because of the ability to integrate over longer time periods.

[29] Recent high-speed measurement of sprites [cf. *Cummer et al.*, 2006; *McHarg et al.*, 2007; *Stenbaek-Nielsen and McHarg*, 2008, and references therein] indicate that sprites may initiate at intermediate altitudes and the initiation can be quite complex. Any initial ionization that is generated starts to shield out the imposed electric field and causes focusing and amplification of the fields at the edges of the ionization. At low altitudes (~50 km for sprites) it is
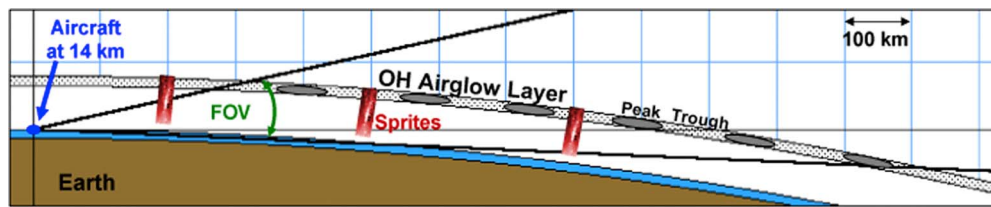
Figure 10. Favorable viewing geometry is needed to observe the correlation between the sprite alignment and the gravity wave structure centered at ~87 km. If observing far away from the storm, e.g., the sprites drawn at 500 to 800 km distance, the tops of sprites are in view and the airglow is bright because of the long path length through the layer. If observing too close to the storm, e.g., sprite at 200 km distance, the camera needs to be tilted up to see the sprite tops and the airglow becomes very faint.

believed that shielding and field focusing processes are responsible for the filamentary structures and streamers [cf. *Pasko et al.*, 1998] seen in sprites. While large scale structures are seen in the gravity wave images there may be smaller scale structures in the areas where the gravity waves are breaking. It is not clear which scale sizes are most important in causing the correlation. The correlation at the tops does not indicate that the sprites are starting at these altitudes as the gravity wave induced changes in density are present at all altitude. Vertical wavelength is an important factor in the gravity wave picture and estimating the vertical wavelength is not possible without wind information. The ratio of horizontal to vertical wavelength describes a tilt in the acoustic-gravity wave. If the vertical wavelength were smaller than the normal sprite altitude span (40–90 km) than there could be multiple peaks and troughs in the region above the causative lightning and the picture may be more complicated. It is not clear if a short vertical wavelength is favorable for seeing a correlation at 80–95 km. With a short vertical wavelength there would be several altitudes where a breakdown could be favored due to the existence of a lower (relative) neutral density. Such a breakdown might want to follow the lowest density path to 80–95 km.

[30] Gravity waves may explain some curious phenomena associated with sprites. For example:

[31] 1) Sprites do not always appear directly over the charge center neutralized in lightning flash

[32] 2) Sprites often repeatedly occur in approximately the same location

[33] 3) Series of sprites sometime have a characteristic tilt or orientation

[34] It is possible that gravity waves are responsible for these observed phenomena. *Pasko et al.* [1997a] indicates that models of gravity wave neutral density structures driven by large 'Mesoscale Convective' storms mimic some of these curious sprite observations. As an example, *Sao Sabbas-Tavares* [2003] has shown that breaking wave amplitudes observed in OH airglow may be large enough to account for the observed horizontal variance in sprite position offsets.

[35] Although avalanche breakdown and consequent streamer formation are now thought to be the primary mechanisms important in sprite formation, at the time of the EXL98 flights there was still debate as to whether the classical breakdown or runaway breakdown [cf. *Taranenko and Roussel-Dupré*, 1996; *Roussel-Dupré and Gurevich*,

1996, and references therein] was most important. We note that for a runaway breakdown process the sprite optical intensity should scale linearly with the neutral density. Thus, if the results of the NIR study show a correlation between the pre-existing gravity wave structures and sprite locations, then the result would strongly favor the classical avalanche breakdown models. If little or no correlation were found, this would enhance the apparent importance of runaway electrons in sprite formation. This was one of the primary motivations for making the NIR measurements.

3.2. Simultaneous NIR and Visible Observations of Sprites and the Sprite Spectrum

[36] There are numerous N_2 neutral and ionized bands in the approximate 900–1700 nm bandpass of the NIR camera. The NIR sprite emissions are primarily from the $\Delta v = 0$ bands of the N_2 1PG. The $[v', v''] = (0,0)$ band of the 1PG is at 1051 nm and is very bright in aurora. In the visible, N_2 1PG are also the brightest sprite emissions from the main body and above [cf. *Morrill et al.*, 1998; *Heavner et al.*, 2000]. For a short time during the mission, the NIR camera was operated using a narrow band 1050 nm filter to try to positively identify emissions from the (0,0) 1PG band, but the results were not conclusive. The filter was undersized for the lens and the combined effects of filter losses and f-number reduction seriously reduced the light gathering capability of the system. Since it was not possible to observe the OH airglow with this filter in place and the probability of capturing a bright sprite was also low, the filtered observations were limited to ~30 min in a single flight. It is possible that there are N_2^+ Meinel contributions to the NIR emissions. However, any interpretation of more than a small percentage of Meinel would not be consistent with mounting spectroscopic evidence. *Mende et al.* [1995], *Hampton et al.* [1996], *Morrill et al.* [1998], *Bucsela et al.* [2003], and others show that the fraction of ionized N_2^+ emissions is small compared to the 1PG emissions (especially in the middle and upper portions of the sprites). Figure 11 presents calculated intensities for several of the N_2 1PG bands that would be detected by the NIR imager. There are a number of assumptions that go into this calculation. First, the effective intensity averaged over a 33 ms frame interval for the 900–1700 nm band is assumed to be one MR. This allows for easy scaling of the results. Second, the data from spectral analysis by *Bucsela et al.* [2003] gives a measure of the vibrational populations
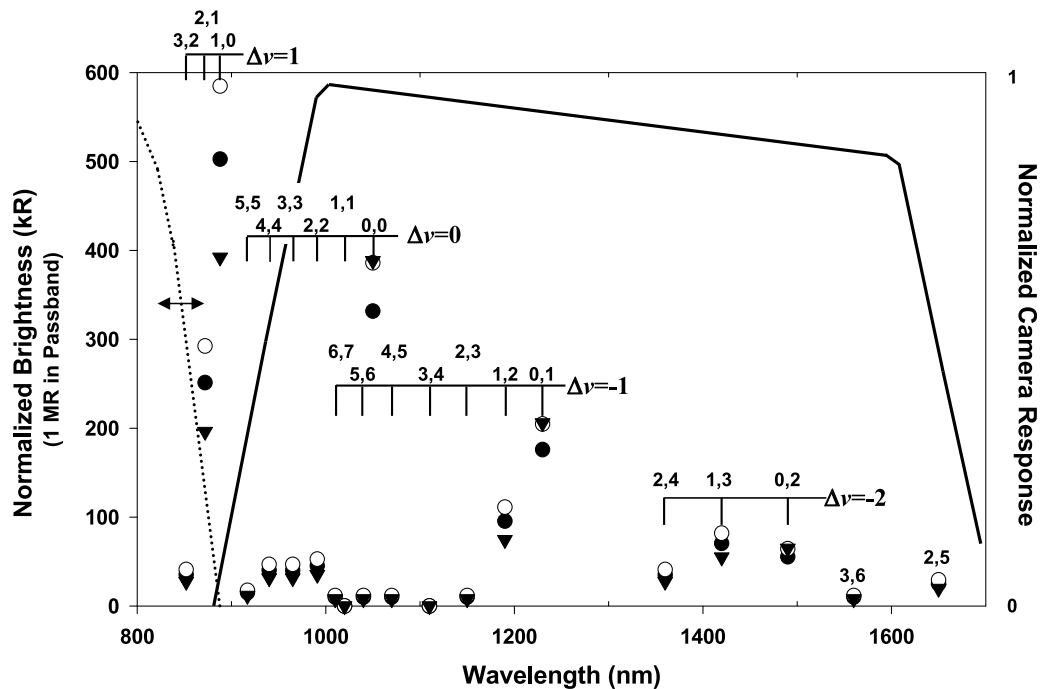
Figure 11. Estimated brightness of various N2 first positive bands in the near-infrared assuming 1 MR between 900 and 1700 nm. N_2 B-state vibrational populations are from *Bucsela et al.* [2003] except for the $v' = 0$ level. The solid circles (empty circles, solid triangles) are for the assumption that the $v' = 0$ population equals 1.0 (0.75, 1.5) times the $v' = 1$ populations. An approximate passband for the EXL98 NIR imager is shown along with a hypothetical band-edge (dashed line) of a visible imager.

of the N_2 B-states. The caveat here is that these data are from a different sprite and from one specific altitude (~65 km). The relative populations, with $v' = 1$ normalized to unity, are given in Table 2. There is no experimental information on the filling of the $v' = 0$ level, so we have plotted three cases where the population in $v' = 0$ is 0.75, 1, and 1.5 times the population in $v' = 1$. Once assuming the v' level populations, it is possible to calculate the emissions using transition probabilities (tabulated by *Gilmore et al.* [1992]). Only the N_2 1PG bands with emissions greater than 1% of the total (10 kR) are plotted. Also plotted is a (not calibrated) passband for the NIR camera as supplied by the manufacturer and a hypothetical band-edge (dashed line) of a visible imager. The biggest contributions to the NIR camera signal are, in order, the (0,0) band, the (0,1) band, the (1,3) band, the (0,2) band, etc.

[37] At wavelengths just short of the NIR band-pass are the $\Delta v = 1$ bands. These are the brightest of the N_2 1PG emissions for any of the assumed vibrational populations. The dashed line in Figure 11 is an approximate response curve for the visible SIT tube cameras and illustrates a problem. Most of the sprite visible-light (imaging) observations are performed with cameras that are not intensity calibrated outside of the bandpass. The response on the cameras is falling rapidly in the 800 to 900-nm range, unfortunately where the brightest emissions occur. It is impossible to know how much of the $\Delta v = 1$ emissions are included in the observations and in resulting brightness estimates. This can have an effect on subsequent analysis using such images. We note that *Morrill et al.* [1998] in

analysis of 1PG spectra indicates the vibrational populations peak at $v' = 2$, although the authors expressed concern about the measured (1,0) intensity as this was on the edge of the spectrographs passband. In later analysis, with different data, *Bucsela et al.* [2003] show that the peak at $v' = 2$ was indeed a result of under-estimating the (1,0) emissions. Also, *Heavner et al.* [2000] attempted to estimate the energy deposited in the mesosphere from measured sprite spectra [*Bucsela et al.*, 2003] and total brightness estimates. They arrived at an energy estimate that appeared to exceed the total electrostatic energy available from the causative lightning [*Sentman et al.*, 2003], most of the error in this calculation resulted from early electron temperature estimates (~1 eV) that were too low, e.g., from *Green et al.* [1996]. Since most of our understanding of sprites comes from interpretation optical images, the above is a strong

Table 2. Normalized $N_2(B)$ Vibrational Population Levels Used to Generate Figure 11

B-State Vibrational Level v'	Relative Population $v' = 1$ Normalized to Unity
1	1
2	0.69
3	0.27
4	0.23
5	0.15
6	0.12
7	0.05

case arguing for better quality observations of the N_2 1PG bands that have the most optical energy, i.e., those in the 800–1250 nm range.

[38] We estimate the brightness of the OH airglow to be close to 10^6 Rayleighs (1 MR) near the horizon and most of the measured sprite emissions were as bright as or brighter than the airglow. This ~1 MR intensity is significant and may be greater than the intensity in the visible range. Published estimates for the brightness of sprites vary greatly. In part the variability comes from the fact that the early measurements were averaged over different areas, times and bandwidths. *Sentman et al.* [1995] and *Wescott et al.* [1995] gave the first estimates for sprite intensity (averaged in time over one video frame) as 600 kR for the brightest areas with a spatially averaged brightness of 50 kR, while *Armstrong et al.* [1998] shows photometric plots of 339.8 nm emissions (a single band of N_2 2PG averaged over about 1/4 of the area of large sprite) reaching a maximum of 150 kR for about 3 ms. More recent observations of sprites using high speed (10 kframe/s) imagers that time resolve the dynamics of streamer heads indicate the optical brightness exceeds 1 GR [*Stenbaek-Nielsen et al.*, 2007].

4. Summary and Conclusions

[39] The NIR observations during EXL98 were extremely successful, making the first measurements of NIR emissions from sprites and also recording the first evidence of a correlation between acoustic-gravity waves and sprite location. Such a correlation has been theoretically postulated for classical avalanche breakdown mechanisms. Although the correlation between gravity waves and sprites was apparent on only one night of observations, the hydroxyl (OH) airglow measurements indicate the gravity waves are ubiquitous near the large thunderstorms sampled during the mission. This investigation shows that a proper viewing geometry is needed for detecting such a correlation. To do this requires a distance of about 400–800 km from the sprites, to insure that the tops of the observed sprites occur in the OH airglow layer near 87 km altitude.

[40] The observed NIR sprite emissions are primarily from the N_2 1PG band system. Comparing the sprite emissions with the OH airglow indicate the NIR sprite emissions are extremely bright. The NIR sprite emission is brightest in the central body, fainter at the tops, and barely above sensitivity in the tendrils.

[41] Spectral measurements of the $\Delta v = 0$ and $\Delta v = 1$ emissions in the NIR are needed to determine the N_2 (B) $v = 0$ and 1 vibrational populations excited in sprites. The importance of these populations to understanding the kinetic processes associated with sprite formation has been discusses in detail elsewhere [cf. *Morrill and Benesch*, 1996; *Morrill et al.*, 1998; *Bucsela et al.*, 2003; *Sentman et al.*, 2008; *Gordillo-Vázquez*, 2008]. The role of a number of different processes, such as, electron impact excitation, quenching, radiative cascade, and after-glow processes (production by vibrationally excited species) changes with altitude in sprites. *Gordillo-Vázquez* [2010] in a kinetic sprite emission model, indicates the $v = 0$ and 1 population levels are particularly sensitive to these processes and these populations represent a significant portion of the total N_2

(B) vibrational distribution. Spectroscopic measurements of the entire N_2 (B) vibrational band system (1PG) will help clarify the relative importance of each of the processes. The EXL98 NIR and visible comparisons imply a change in the central core-to-top brightness ratio in sprites and could indicate a change in the relative vibration populations in the two regions. The change in population ratio, in turn, implies changes in the role of the various processes that are occurring at different altitudes. Because of saturation in the visible instruments this conclusion needs to be confirmed by future observations.

References

Armstrong, R. A., J. A. Shorter, M. J. Taylor, D. M. Suszcynsky, W. A. Lyons, and L. S. Jeong (1998), Photometric measurements in the SPRITES '95 & '96 campaigns, nitrogen second positive (399.8 nm) and first negative (427.8 nm) emission, *J. Atmos. Sol. Terr. Phys.*, 60, 787, doi:10.1016/S1364-6826(98)00026-1.

Baker, D. J., and A. T. Stair Jr. (1988), Rocket measurements of the altitude distributions of the hydroxyl airglow, *Phys. Scr.*, 37, 611, doi:10.1088/0031-8949/37/4/021.

Bowles, J., C. Siefring, J. Morrill, P. Bernhardt, D. Sentman, D. Moudry, E. Bucsela, D. Osborne, E. Wescott, and M. Heavner (1998), Do sprites sometimes connect to the cloud tops?, *Eos Trans. AGU*, 79(45), Fall Meet. Suppl., F164.

Bucsela, E., J. S. Morrill, M. J. Heavner, C. L. Siefring, S. Berg, D. L. Hampton, D. R. Moudry, E. M. Wescott, and D. D. Sentman (2003), $N_2(B^3\Pi_g)$ and $N_2^+(A^2\Pi_u)$ vibrational distributions observed in sprites, *J. Atmos. Sol. Terr. Phys.*, 65, 583, doi:10.1016/S1364-6826(02)00316-4.

Chamberlain, J. W. (1995), *Classics in Geophysics—Physics of the Aurora and Airglow*, AGU, Washington, D. C.

Cummer, S. A., N. Jaugey, J. Li, W. A. Lyons, T. E. Nelson, and E. A. Gerken (2006), Submillisecond imaging of sprite development and structure, *Geophys. Res. Lett.*, 33, L04104, doi:10.1029/2005GL024969.

Eckermann, S. D., and P. Preusse (1999), Global measurements of stratospheric mountain waves from space, *Science*, 286, 1534, doi:10.1126/science.286.5444.1534.

Fernsler, R. F., and H. L. Rowland (1996), Models of lightning-produced sprites and elves, *J. Geophys. Res.*, 101(D23), 29,653, doi:10.1029/96JD02159.

Freund, J. T., and F. Jacka (1979), Structure in the 557.7 nm forbidden (OI) airglow, *J. Atmos. Terr. Phys.*, 41, 25, doi:10.1016/0021-9169(79)90043-6.

Gerken, E. A., U. S. Inan, C. P. Barrington-Leigh, and M. Stanley (1998), Results from a new telescopic imager: A survey of sprite structures, *Eos Trans. AGU*, 79(45), Fall Meet. Suppl., F137.

Gilmore, F. R., R. R. Laher, and P. J. Espy (1992), Frank-Condon factors, r-centroids, electronic transition moments, and Einstein coefficients for many nitrogen and oxygen systems, *J. Phys. Chem. Ref. Data*, 21, 1005, doi:10.1063/1.555910.

Gordillo-Vázquez, F. J. (2008), Air plasma kinetics under the influence of sprites, *J. Phys. D Appl. Phys.*, 41, 234016, doi:10.1088/0022-3727/41/23/234016.

Gordillo-Vázquez, F. J. (2010), Vibrational kinetics of air plasmas induced by sprites, *J. Geophys. Res.*, 115, A00E25, doi:10.1029/2009JA014688.

Green, B. D., M. E. Fraser, W. T. Rawlins, L. Jeong, W. A. M. Blumberg, S. B. Mende, G. R. Swenson, D. L. Hampton, E. M. Wescott, and D. D. Sentman (1996), Molecular excitation in sprites, *Geophys. Res. Lett.*, 23(16), 2161, doi:10.1029/96GL02071.

Hampton, D. L., M. J. Heavner, E. M. Wescott, and D. D. Sentman (1996), Optical spectral characteristics of sprites, *Geophys. Res. Lett.*, 23(1), 89, doi:10.1029/95GL03587.

Heavner, M. J. (2000), Optical spectroscopic observations of sprites, blue jets, and elves: Inferred microphysical processes and their macrophysical implications, Ph.D. thesis, Univ. of Alaska Fairbanks, Fairbanks.

Heavner, M. J., D. D. Sentman, D. R. Moudry, E. M. Wescott, C. L. Siefring, J. S. Morrill, and E. J. Bucsela (2000), Sprites, blue jets, and elves: Optical evidence of energy transport across the stratopause, in *Atmospheric Science Across the Stratopause, Geophys. Monogr. Ser.*, vol. 123, edited by D. E. Siskind, S. D. Eckermann, and M. E. Summers, p. 69, AGU, Washington, D. C.

Heavner, M. J., J. S. Morrill, C. Siefring, D. D. Sentman, D. R. Moudry, E. M. Wescott, and E. J. Bucsela (2010), Near-ultraviolet and blue spectral observations of sprites in the 320–460 nm region: N_2 (2 PG) emissions, *J. Geophys. Res.*, *115*, A00E44, doi:10.1029/2009JA014858.

Hines, C. O. (1968), A possible source of waves in noctilucent clouds, *J. Atmos. Sci.*, *25*, 937, doi:10.1175/1520-0469(1968)025<0937:APSOWI>2.0.CO;2.

Hung, R. J., T. Phan, and R. E. Smith (1979), Coupling of ionosphere and troposphere during the occurrence of isolated tornadoes on November 20, 1973, *J. Geophys. Res.*, *84*(A4), 1261, doi:10.1029/JA084iA04p01261.

Llewellyn, E. J., B. H. Long, and B. H. Solheim (1978), The quenching of OH* in the atmosphere, *Planet. Space Sci.*, *26*, 525, doi:10.1016/0032-0633(78)90043-0.

McHarg, M. G., H. C. Stenbaek-Nielsen, and T. Kammae (2007), Observations of streamer formation in sprites, *Geophys. Res. Lett.*, *34*, L06804, doi:10.1029/2006GL027854.

Mende, S. B., R. L. Rairden, G. R. Swenson, and W. A. Lyons (1995), Sprite spectra; N_2 1 PG band identification, *Geophys. Res. Lett.*, *22* (19), 2633, doi:10.1029/95GL02827.

Morrill, J. S., and W. M. Benesch (1996), Auroral N_2 emissions and the effect of collisional processes on N_2 triplet state vibrational populations, *J. Geophys. Res.*, *101*(A1), 261, doi:10.1029/95JA02835.

Morrill, J. S., E. J. Bucsela, V. P. Pasko, S. L. Berg, W. M. Benesch, E. M. Wescott, and M. J. Heavner (1998), Time resolved N_2 state vibrational populations and emissions associated with red sprites, *J. Atmos. Sol. Terr. Phys.*, *60*, 811, doi:10.1016/S1364-6826(98)00031-5.

Morrill, J., et al. (2002), Electron energy and electric field estimates in sprites derived from ionized and neutral N_2 emissions, *Geophys. Res. Lett.*, *29*(10), 1462, doi:10.1029/2001GL014018.

Pasko, V. P., U. S. Inan, and T. F. Bell (1997a), Sprites as evidence of vertical gravity wave structures above mesoscale thunderstorms, *Geophys. Res. Lett.*, *24*(14), 1735, doi:10.1029/97GL01607.

Pasko, V. P., U. S. Inan, T. F. Bell, and Y. N. Taranenko (1997b), Sprites produced by quasi-electrostatic heating and ionization in the lower ionosphere, *J. Geophys. Res.*, *102*(A3), 4529, doi:10.1029/96JA03528.

Pasko, V. P., U. S. Inan, and T. F. Bell (1998), Spatial structure of sprites, *Geophys. Res. Lett.*, *25*(12), 2123, doi:10.1029/98GL01242.

Raizer, Y. P., G. M. Milikh, M. N. Shneider, and S. V. Novakovski (1998), Long streamers in the upper atmosphere above thundercloud, *J. Phys. D Appl. Phys.*, *31*, 3255, doi:10.1088/0022-3727/31/22/014.

Roach, F. E. and A.B. Meinel (1955), The height of the nightglow by the Van Rhijn method, *Astrophys. J.*, *121*, 530, doi:101086/146115.

Röttger, J. (1977), Traveling disturbances in the equatorial ionosphere and their association with penetrative cumulus clouds, *J. Atmos. Terr. Phys.*, *39*, 987, doi:10.1016/0021-9169(77)90007-1.

Roussel-Dupré, R., and A. V. Gurevich (1996), On runaway breakdown and upward propagating discharges, *J. Geophys. Res.*, *101*(A2), 2297, doi:10.1029/95JA03278.

Rowland, H. L. (1998), Theories and simulations of elves, sprites and blue jets, *J. Atmos. Sol. Terr. Phys.*, *60*, 831, doi:10.1016/S1364-6826 (98)00034-0.

Rowland, H. L., R. F. Fernsler, and P. A. Bernhardt (1996), Breakdown of the neutral atmosphere in the *D* region due to lightning driven electromagnetic pulses, *J. Geophys. Res.*, *101*(A4), 7935, doi:10.1029/95JA03519.

Sao Sabbas-Tavares, F. (2003), Role of conductivity spatial structure in determining the location of sprite initiation, Ph.D. thesis, Univ. of Alaska Fairbanks, Fairbanks.

Sentman, D. D., E. M. Wescott, D. L. Osborne, D. L. Hampton, and M. J. Heavner (1995), Preliminary results from the Sprites94 Aircraft Campaign: 1. Red sprites, *Geophys. Res. Lett.*, *22*(10), 1205, doi:10.1029/95GL00583.

Sentman, D. D., E. M. Wescott, R. H. Picard, J. R. Winick, H. C. Stenbaek-Nielsen, E. M. Dewan, D. R. Moudry, F. T. Sao Sabbas, M. J. Heavner, and J. Morrill (2003), Simultaneous observations of mesospheric gravity waves and sprites generated by a midwestern thunderstorm, *J. Atmos. Sol. Terr. Phys.*, *65*, 537, doi:10.1016/S1364-6826(02)00328-0.

Sentman, D. D., H. C. Stenbaek-Nielsen, M. G. McHarg, and J. S. Morrill (2008), Plasma chemistry of sprite streamers, *J. Geophys. Res.*, *113*, D11112, doi:10.1029/2007JD008941.

Sharma, R. D. (1985), Infrared airglow, in *Handbook of Geophysics and the Space Environment*, vol. 1, edited by A. Jursa, p. 31-1, Air Force Geophys. Lab., Hanscom Air Force Base, Mass.

Stenbaek-Nielsen, H. C., and M. G. McHarg (2008), High time-resolution sprite imaging: Observations and implications, *J. Phys. D Appl. Phys.*, *41*, 234009, doi:10.1088/0022-3727/41/23/234009.

Stenbaek-Nielsen, H. C., M. G. McHarg, T. Kammae, and D. D. Sentman (2007), Observed emission rates in sprite streamer heads, *Geophys. Res. Lett.*, *34*, L11105, doi:10.1029/2007GL029881.

Suszcynsky, D. M., R. A. Roussel-Dupré, W. A. Lyons, and R. A. Armstrong (1998), Blue-light imagery and photometry of sprites, *J. Atmos. Sol. Terr. Phys.*, *60*, 801, doi:10.1016/S1364-6826(98)00027-3.

Taranenko, Y., and R. Roussel-Dupré (1996), High altitude discharges and gamma-ray flashes: A manifestation of runaway air breakdown, *Geophys. Res. Lett.*, *23*(5), 571, doi:10.1029/95GL03502.

Tarasick, D. W., and G. G. Shepherd (1992a), Effects of gravity waves on complex airglow chemistries: 1. $O_2(b^1\Sigma_g^+)$ emission, *J. Geophys. Res.*, *97* (A3), 3185, doi:10.1029/91JA02579.

Tarasick, D. W., and G. G. Shepherd (1992b), Effects of gravity waves on complex airglow chemistries: 2. OH emission, *J. Geophys. Res.*, *97*(A3), 3195, doi:10.1029/91JA02580.

Taylor, M. J., and M. A. Hapgood (1988), Identification of a thunderstorm as a source of short period gravity waves in the upper atmosphere nightglow emissions, *Planet. Space Sci.*, *36*, 975, doi:10.1016/0032-0633(88) 90035-9.

Taylor, M. J., P. J. Espy, D. J. Baker, R. J. Sica, P. C. Neal, and W. R. Pendleton Jr. (1991), Simultaneous intensity, temperature and imaging measurements of short period wave structures in the OH nightglow emission, *Planet. Space Sci.*, *39*, 1171, doi:10.1016/0032-0633(91)90169-B.

Taylor, M. J., V. Taylor, and R. Edwards (1995), An investigation of thunderstorms as a source of short period mesospheric gravity waves, in *The Upper Mesosphere and Lower Thermosphere: Review of Experiment and Theory, Geophys. Monogr. Ser.*, vol. 87, edited by R. M. Johnson and T. L. Killeen, p. 177, AGU, Washington, D. C.

Taylor, M. J., P.-D. Pautet, A. F. Medeiros, R. A. Buriti, J. Fechine, D. C. Fritts, S. L. Vadas, H. Takahashi, and F. T. Sao Sabbas (2009), Characteristics of mesospheric gravity waves near the magnetic equator, Brazil during the SpreadFEx campaign, *Ann. Geophys.*, *27*, 461, doi:10.5194/angeo-27-461-2009.

Vadas, S. L., M. J. Taylor, P.-D. Pautet, P. A. Stamus, D. C. Fritts, H.-L. Liu, F. T. Sao Sabbas, V. T. Rampinelli, P. Batista, and H. Takahashi (2009), Convection: The likely source of the medium-scale gravity waves observed in the OH airglow layer near Brasilia, Brazil, during the SpreadFEx campaign, *Ann. Geophys.*, *27*, 231, doi:10.5194/angeo-27-231-2009.

Walterscheid, R. L., G. Schubert, and M. P. Hickey (1994), Comparison of theories for gravity wave induced fluctuations in airglow emissions, *J. Geophys. Res.*, *99*(A3), 3935, doi:10.1029/93JA03312.

Wescott, E. M., D. Sentman, D. Osborne, D. Hampton, and M. Heavner (1995), Preliminary results from the Sprites94 Aircraft Campaign: 2. Blue jets, *Geophys. Res. Lett.*, *22*(10), 1209, doi:10.1029/95GL00582.

Wescott, E. M., D. D. Sentman, H. C. Stenbaek-Nielsen, P. Huet, M. J. Heavner, and D. Moudry (2001), New evidence for the brightness and ionization of blue starters and blue jets, *J. Geophys. Res.*, *106*(A10), 21,549, doi:10.1029/2000JA000429.

M. J. Heavner, Los Alamos National Laboratory, Los Alamos, NM 87545, USA.

J. S. Morrill, E. O. Hulburt Center for Space Research, Naval Research Laboratory, Washington, DC 20375, USA.

D. D. Sentman, Geophysical Institute, University of Alaska Fairbanks, Fairbanks, AK 99775, USA.

C. L. Siefring, Plasma Physics Division, Naval Research Laboratory, Washington, DC 20375, USA. (siefring@ccs.nrl.navy.mil)